Journal of Electric Propulsion

RESEARCH Open Access

Characterization of the performance of a RIT-10 and rf-neutralizer for an ABEP system

Jana Zorn[1*], Kalle J. Bräumer[1], Rodrigo S. Rodriguez[1], Andreas R. Wölki[1], Konstantin Keil[1], Anna Komjagin[1], Fiene B. Bremer[1], Aaron Hellbert[1], Mathis Reuß-Hennschen[1], Arnold Kaufmann[1], Johannes Krempel-Hesse[1], Limei Chen[1], Kristof Holste[1] and Peter J. Klar[1]

*Correspondence:
Jana Zorn
jana.zorn@physik.uni-giessen.de
[1]Institute of Experimental Physics I, Justus Liebig University of Giessen, Heinrich-Buff-Ring 16, 35392 Giessen, Hesse, Germany

Abstract

We investigated a RIT-10 ion thruster and a radio-frequency neutralizer using molecular oxygen, molecular nitrogen and mixtures of both gases as propellants to assess their suitability as components for an air-breathing electric propulsion (ABEP) system. A combination of diagnostics - including Langmuir probes, optical emission spectroscopy (OES), Faraday cups, retarding potential analyzers (RPA), mass spectrometry and Raman spectroscopy - was used to characterize the plasma parameters, plume properties and material contamination. A comparison was made between the experimental results for the single gases and a corresponding global model. Our results show that the dissociation of the molecules and chemical reactions taking place in the plasma have a significant impact on the performance of both tested devices and thus need to be assessed for all operating points. Chemical reactions between oxygen and different material surfaces are identified and safe operating points established. A general optimization strategy to improve the performance of both devices is suggested - an essential requirement for successful missions using ABEP systems. The findings provide critical insight into material suitability and operational regimes for ABEP systems. An optimization based on an in-depth understanding of all parameters involved is only possible by combining multiple diagnostic tools and global modeling.

Keywords ABEP, RIT, rf-neutralizer, Diagnostics, Langmuir probe, RPA, Mass spectrometry, Raman spectroscopy, OES, Oxygen, Nitrogen, Global model

Introduction

The development of a functional and reliable air-breathing electric propulsion (ABEP) system poses substantial physical and engineering challenges. Designed for satellites in very low Earth orbit (VLEO, 150–250 km altitude), such systems collect and compress residual atmospheric gases - primarily atomic oxygen (ATOX) and molecular nitrogen - to use as propellant [1]. This concept enables virtually unlimited propellant supply, potentially extending mission lifetimes, provided the generated thrust exceeds atmospheric drag. However, highly variable atmospheric conditions and the resulting

fluctuating drag make consistent and efficient operation difficult. Additionally, the interaction of ATOX with spacecraft materials leads to degradation effects that must be carefully addressed.

Thorough characterization of the propulsion system under all relevant operating conditions is essential. However, using ATOX as propellant, which is the most common species at these orbital altitudes, is not easily achievable under laboratory conditions. Furthermore, the recombination rate of ATOX to O_2 inside the intake is unknown and thus also the actual fraction of ATOX inside the propulsion system. Hence, candidate ABEP systems are mostly investigated using solely molecular oxygen (O_2) and nitrogen (N_2) or their mixtures as propellant. Molecular propellants, unlike inert gases, introduce additional complexities such as dissociation, vibrational and rotational excitation, and chemical reactivity - especially in the case of ATOX. These effects influence both performance and lifetime of the thruster. Therefore, a comprehensive diagnostic approach is required to fully capture the physical and chemical phenomena involved and to define the operational envelope of the system.

Among the key parameters for characterizing a thruster or rf-neutralizer are the plume parameters and plasma parameters, i.e., composition, divergence angle of the plume, ion energy, ion and electron density $n_{\mathrm{i,e}}$, electron temperature T_{e} and the ion and neutral gas temperature $T_{\mathrm{i,g}}$. They determine the performance and also the material degradation. Some performance investigations, plasma parameter measurements and material degradation studies were already performed by other groups using Hall thrusters, multicusped thrusters, Helicon Hall thrusters or inductively coupled plasma sources using inert gases, oxygen, nitrogen or oxygen-nitrogen mixtures [2–11]. Mostly combinations of thrust balances or force probes, Langmuir probes, retarding potential analyzers and Faraday cups are used as diagnostic tools. However, some of these measurements are only conducted separately instead of combined and in a small operating regime of the thruster only. The Langmuir measurements are mostly conducted in the plume instead of the discharge region. Thus, the main discharge parameters are mostly unknown.

The additional dissociation processes occurring in molecular propellants result in a mixture of atoms and molecules within the thruster. Furthermore, molecular species exhibit rotational and vibrational energy losses, which contribute to increased power consumption. Consequently, the ions' atomic-to-molecular number density ratio, $n_{\mathrm{atomic}}/n_{\mathrm{molecular}}$, is a critical parameter—both in the plume for accurate thrust prediction and in the discharge chamber for a comprehensive assessment of thruster performance. This is of utmost importance, since the balance between thrust and drag for ABEP is very sensitive. The measurement of the plume composition has not been experimentally performed by most other groups. Overestimating the produced thrust can lead to a failure of the entire mission. Additionally the kinetic energy of the ions E_{kin} and the divergence angle of the plume α_{div} are important parameters to precisely calculate the thrust and also define highly efficient points of operation. Finally, the extracted current of the rf-neutralizer must be investigated as a function of operating conditions. If the extracted electron (and negative ion) current is lower than the extracted positive ion current from the thruster, the whole system will not be functioning properly. Currently, only a limited number of alternative neutralizer technologies are capable of operating reliably with alternative propellants, especially oxygen [6, 12, 13]. Only Tisaev et al. [6] characterized a microwave neutralizer operating with oxygen as propellant using

multiple diagnostics, such as Langmuir probes and materials investigation, to better understand its performance behavior.

In order to better understand the highly complex processes involved when using mixtures of two molecular propellants, it is reasonable to first investigate the individual gases rather than starting directly with the mixture. After a full understanding of all processes, both experimental and modeling, in the two pure molecular propellants the mixtures can be addressed. This is further illustrated in the roadmap presented in Fig. 1, where the red box serves as a symbolic representation of the part presented here.

This paper is structured as follows: In Sect. 2 the experimental setup for characterizing the thruster and neutralizer is described. Section 3 explains the global model used to simulate the thruster and neutralizer using O_2 and N_2 as propellants. In Sect. 4 the results are presented. First, the results of plume measurements for the RIT-10 are described and discussed, utilizing an example that illustrates the high complexity of gas mixtures of molecular propellants (O_2/N_2). Subsequently, the plasma parameters were separately measured for O_2 or N_2 as propellant. Following this, the impact of varying excitation frequencies on the plasma parameters of the rf-neutralizer using the single gases is discussed. Additional material investigations of different catcher materials were conducted and the results are shown. Finally, the plasma parameters from the thruster, the neutralizer and the results from the global model, as well as results from optical emission spectroscopy (OES) measurements are compared. In Sect. 5 a conclusion is drawn.

Experimental setup

The experiments were conducted in the vacuum test facility Obelix. A schematic image of the setup is shown in Fig. 2 and an overview of the used diagnostics is given in Table 1. The facility includes a main chamber with a diameter of 1.6 m and a length of 2.5 m. It is equipped with a turbo-molecular pump and a cryogenic pump, providing a combined pumping speed of approximately 30 000 l/s for nitrogen. This yields a background

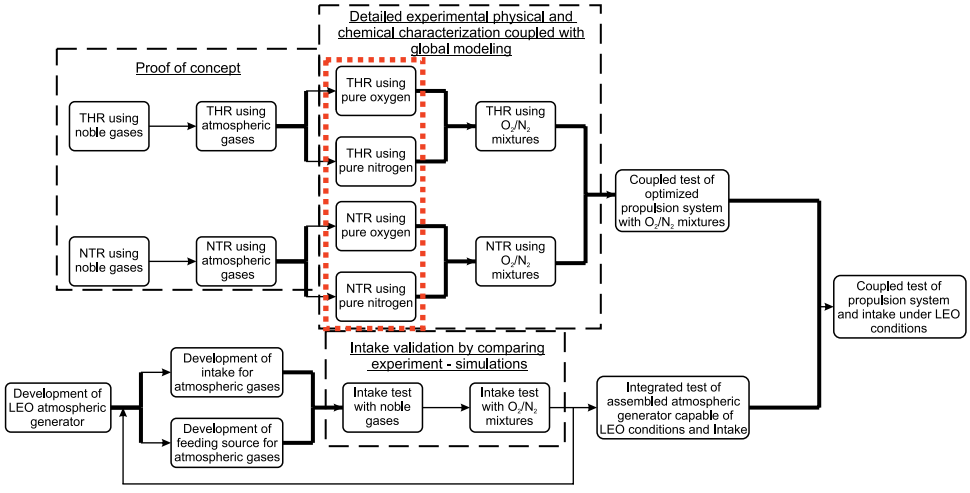

Fig. 1 Roadmap towards a fully integrated test of an abep system. The acronym thr is an shorthand for thruster, while ntr is an indicator for neutralizer. The red box indicates the investigated step in this paper. Before characterizing the system with complex mixtures of molecular and atomic gases the physical and chemical behavior of the pure molecular gases (only oxygen and only nitrogen) must be investigated and compared with global models

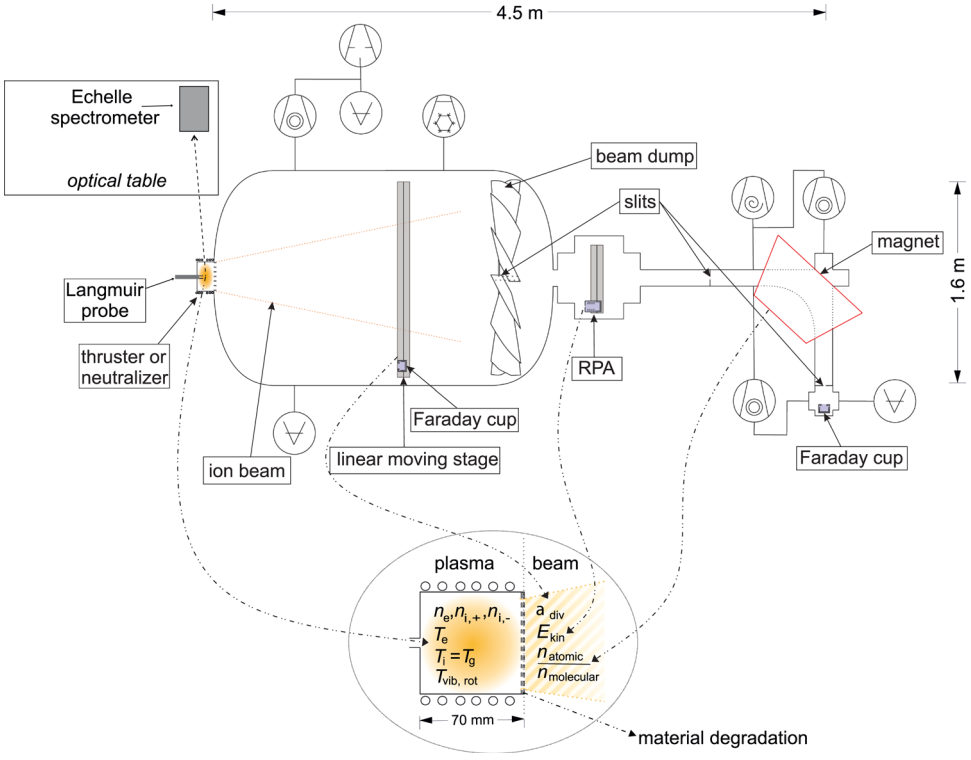

Fig. 2 Schematic drawing of the experimental setup used for characterizing plasma parameters and plume properties of a radio-frequency ion thruster (RIT-10) and an rf-neutralizer. The configuration includes the vacuum chamber equipped with optical diagnostics (echelle spectrometer), in-beam diagnostics (faraday cup, rpa, magnetic sector analyzer), and in-situ plasma diagnostics (Langmuir probe). Key measurement locations for parameters such as ion/electron density (n_e, n_i), temperatures (T_e, $T_{i,g}$), plume divergence (α_{div}), and ion energy (E_{kin}) are indicated. The thruster and neutralizer are mounted externally to improve optical access. The beam dump includes an aperture that allows a small portion of the ion beam to pass through for downstream diagnostics by magnetic sector analyzer and faraday cup

Table 1 Overview of diagnostics and their purpose

Diagnostic tool	Measured quantity	Location
Faraday cup	Beam profile, Beam divergence	Beam
RPA	Ion energy distribution	Beam
Magnetic sector analyzer	Ion mass-to-charge ratio	Beam
Langmuir double probe	Plasma parameters ($n_{e,i}$, T_e)	Discharge plasma
OES	Excitation states, $T_{vibrational}$, $T_{rotional}$	Discharge plasma
Raman spectroscopy	Surface composition, material degradation	Ion catcher surface

pressure during the experiments between $7 \cdot 10^{-7}$ mbar and $2 \cdot 10^{-5}$ mbar, depending on the mass flow rate.

An additional beamline is connected to the end of the chamber and leads to a 90° magnetic sector analyzer for mass spectrometry. This analyzer features an electromagnet capable of generating magnetic fields up to 1 T enabling mass-to-charge ratio analysis up to $2.5\,\mathrm{MeV} \cdot \mathrm{amu}$. Slits with a width of 10 mm in the focusing plane improve measurement accuracy. A Faraday cup at the end of the beamline is used for ion detection. The total length of the beamline from the thruster exit to the Faraday cup is about 5 m. The magnetic sector analyzer is further equipped with two additional turbo-molecular pumps with a total pumping speed of 66 l/s, to ensure low background pressure during operation.

A retarding potential analyzer (RPA) is positioned in front of the magnetic sector analyzer to measure the ion energy distribution along the beam axis. It is mounted on a motorized linear stage, allowing it to be moved in and out of the beam path. The distance between the RPA and the thruster exit is approximately 3 m.

In the main chamber, an additional Faraday cup with a 10 mm orifice is mounted on a linear translational stage with a travel range of 700 mm. It is positioned 910 mm away from the thruster exit and perpendicular to the beam direction. It is used to measure the beam profile.

A Langmuir double probe is employed to measure plasma parameters inside both the thruster and the rf-neutralizer. It is mounted at the gas inlet of the device under study and extends into its discharge chamber. The probe surface area is $3.2 \times 10^{-6}\,\mathrm{m}^2$ inside the thruster and $4.88 \times 10^{-6}\,\mathrm{m}^2$ inside the neutralizer.

The optical emission spectra are recorded in the wavelength range from 200 nm to 975 nm using a wavelength- and response-corrected echelle spectrometer (Mechelle ME 5000, Andor Technology Ltd.). An iKon-M DU934 CCD detector is employed. Within this spectral range, the spectral resolution is between $\Delta\lambda = 0.04$ nm and 0.195 nm, with a $\Delta\lambda/\lambda = 5000$. Both the thruster and the neutralizer are flanged to the outside of the vacuum tank for easier optical access to the plasma inside the discharge chamber.

A radio-frequency ion thruster, with a discharge chamber that has a diameter of 10 cm (RIT-10), is used for the experiments. A three-grid system made of titanium and featuring 499 extraction holes is used, enabling extraction currents up to approx. 500 mA for oxygen and nitrogen. The frequency applied to the rf-coil for generating the plasma is between 1.6 MHz and 2 MHz, the extraction voltage is set to 1400 V on the screen grid and −50 V on the acceleration grid. As mass flow controller (MFC) two El-Flow Prestige FG-201CV (20 sccm) from Bronkhorst, calibrated for O_2 and N_2, respectively, are used. The accuracy is 0.5% of the measured value plus 0.1% of the maximum value of the MFC. This gives a total accuracy of better than 1% for all used mass flow rates for providing propellant to the thruster.

An rf-neutralizer, similar in design to a RIT-4, is used in the setup. As an ion catcher, a molybdenum orifice plate with seven extraction holes (each 3.5 mm in diameter) is employed. A cylindrical anode made of graphite foil, 80 mm in diameter and positioned 54 mm behind the orifice plate, is used for extracting electrons. Multiple holes in the anode are included to reduce the neutral gas density between the anode and the neutralizer. The anode is biased at + 35 V, while the ion catcher is held at ground potential (0 V). The excitation frequency is varied between 1.3 and 2.0 MHz during operation. The same MFCs for providing propellant are used as for the thruster. For the smaller mass flow rates of the neutralizer the accuracy is better than 2.5%.

The electrical wiring of the used thruster, neutralizer, Faraday cups and RPA can be seen in Fig. 3. A more detailed explanation of the RIT can be found in Ref. [14], while the rf-neutralizer is explained in Ref. [15].

Global modeling

The global model consists of a set of ordinary differential equations (ODEs) that describe the time evolution of ion and neutral gas densities (n_i, n_g), as well as the electron and gas temperatures (T_e, T_g). It is based on the model proposed by Grondein et al., which builds on the work of Chabert et al. and extends it to diatomic gases [16, 17].

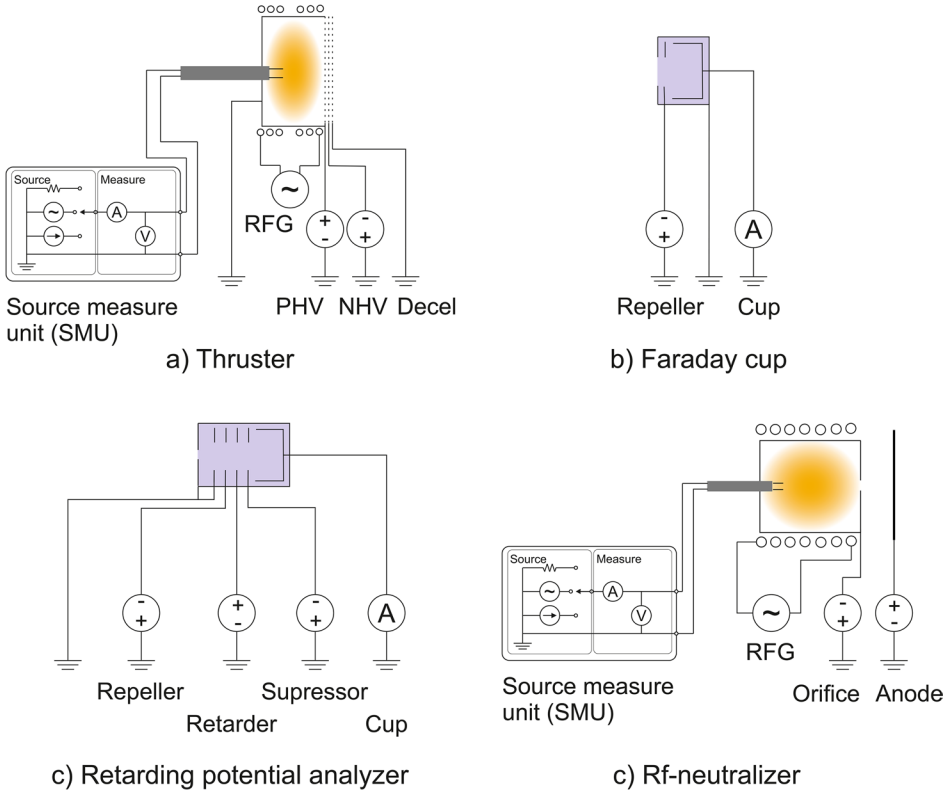

Fig. 3 Electrical wiring of (**a**) Thruster, (**b**) Faraday cups, (**c**) rpa, and (**d**) rf-neutralizer. rfg denotes the radio-frequency generator, PHV the positive high voltage on the first grid, NHV the negative high voltage on the second grid, and decel the third grid

The computational sequence is illustrated in Fig. 4. Initial input includes the RF power (P_{RF}), discharge chamber dimensions, ion and gas transparency of the grid system, and both geometry and electrical properties of the RF coil. The system of ODEs is then solved numerically to obtain particle densities and temperatures. These values are then used to compute the resulting ion beam current (I_{beam}), which is compared against a predefined target current ($I_{\mathrm{beam,s}}$). If the deviation exceeds a specified threshold, the RF power is adjusted and the process of solving the ODEs is repeated. Once the calculated current matches the target current and fulfills the predefined convergence criteria, the computation is terminated.

There are two separate models for nitrogen and oxygen which differ in the particles they contain and the possible reactions between them. The particle species included in the nitrogen-model are: e^-, $\mathrm{N_2}$, N, $\mathrm{N_2^+}$ and $\mathrm{N^+}$ whereas the oxygen-model contains: e^-, $\mathrm{O_2}$, O, $\mathrm{O_2^+}$, $\mathrm{O^+}$, $\mathrm{O_2(a^1\Delta_g)}$, $\mathrm{O_2^-}$ and $\mathrm{O^-}$. The singlet state of molecular oxygen, $\mathrm{O_2(a^1\Delta_g)}$, is treated as a separate species due to its significant role in the formation of negative oxygen ions ($\mathrm{O^-}$).

These species participate in a variety of excitation, dissociation and collisional processes, which are listed in Tables 2 and 3. Since the excitation of molecular and atomic species can occur into several different energy levels, it is described by a single effective rate coefficient - which is a mean value of individual rate coefficients weighted by their respective energy - and an electron temperature-dependent excitation threshold for each species. The effective rate coefficient is defined as the sum of the individual reaction rate

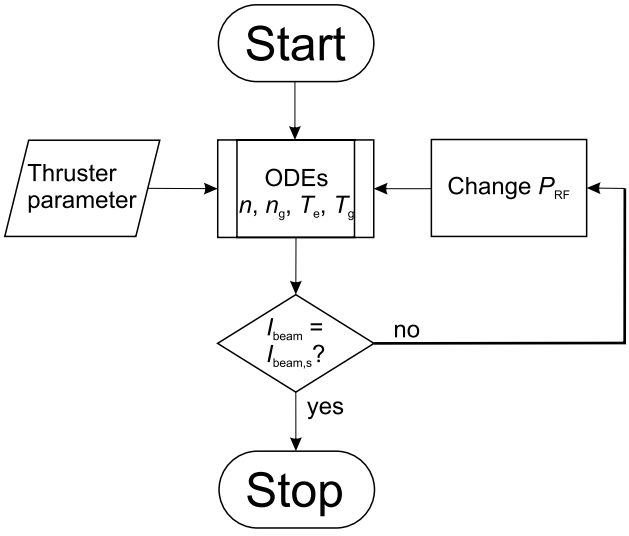

Fig. 4 Sequence diagram of the global model used to simulate the operation of a radio-frequency ion thruster and rf-neutralizer. Input parameters such as rf power, chamber dimensions, and grid transparency are used to solve the system of differential equations describing particle densities and temperatures. The resulting ion beam current is compared to a target setpoint, and the rf power is iteratively adjusted until convergence is reached

Table 2 Set of chemical reactions used in the global model for describing the occurring related species in a nitrogen plasma. Sources refer to the cross sections or rate coefficients used in each case. Wall recombination rates were calculated directly using the corresponding terms in Eqs. (9) and (10) of Ref. [16], rather than via reaction rate coefficients

Reaction	Description	Reference
$e^- + N_2 \rightarrow e^- + N_2^*$	Excitation N_2	[18]
$e^- + N \rightarrow e^- + N^*$	Excitation N	[19]
$e^- + N_2 \rightarrow e^- + N_2$	Elastic momentum transfer N_2	[20]
$e^- + N \rightarrow e^- + N$	Elastic momentum transfer N	[19]
$e^- + N_2 \rightarrow e^- + N_2$	Elastic collision N_2	[20]
$e^- + N \rightarrow e^- + N$	Elastic collision N	[19]
$e^- + N_2 \rightarrow 2e^- + N_2^+$	Ionization N_2	[18]
$e^- + N \rightarrow 2e^- + N^+$	Ionization N	[19]
$e^- + N_2 \rightarrow 2e^- + N^+ + N$	Dissociative ionization	[20]
$e^- + N_2^+ \rightarrow 2e^- + 2N^+$	Dissociative ionization ion	[21]
$e^- + N_2 \rightarrow e^- + 2N$	Dissociation	[22]
$e^- + N_2^+ \rightarrow e^- + N^+ + N$	Dissociation ion	[21]
$e^- + N_2^+ \rightarrow 2N$	Dissociative ion attachment	[23]
$N_2^+ + \text{Wall} \rightarrow N_2$	Surface recombination N_2^+	-
$N^+ + \text{Wall} \rightarrow N$	Surface recombination N^+	-
$N + \text{Wall} \rightarrow \frac{1}{2}N_2$	Surface recombination N	-

coefficients, while the threshold energy is computed as a weighted average of the individual excitation thresholds, weighted by their respective rate coefficients.

Tables 2 and 3 already demonstrate the complexity of models for the diatomic propellants O_2 or N_2 alone in terms of possible reactions and arising species inside the plasma. Following the idea of our roadmap in Fig. 1, it is essential to fully understand the diatomic elemental propellants and to describe them correctly prior to addressing the even more complex N_2/O_2 mixtures which show a much larger number of possible

Table 3 Set of chemical reactions used in the global model for describing the occurring species of an oxygen plasma. Sources refer to the cross sections or rate coefficients used in each case. Wall recombination rates were calculated directly using the corresponding terms in Eq. (9) and (10) of Ref. [16], rather than via reaction rate coefficients

Reaction	Description	Reference
$e^- + O_2 \rightarrow e^- + O_2^*$	Excitation O_2	[24]
$e^- + O \rightarrow e^- + O^*$	Excitation O	[25]
$e^- + O_2 \rightarrow e^- + O_2$	Elastic momentum transfer O_2	[26]
$e^- + O \rightarrow e^- + O$	Elastic momentum transfer O	[27]
$e^- + O_2 \rightarrow e^- + O_2$	Elastic collision O_2	[26]
$e^- + O \rightarrow e^- + O$	Elastic collision O	[28]
$e^- + O_2 \rightarrow 2e^- + O_2^+$	Ionization O_2	[18]
$e^- + O \rightarrow 2e^- + O^+$	Ionization O	[29]
$e^- + O_2 \rightarrow 2e^- + O^+ + O$	Dissociative ionization	[24]
$e^- + O_2^+ \rightarrow 2e^- + 2O^+$	Dissociative ionization ion	[30]
$e^- + O_2 \rightarrow e^- + 2O$	Dissociation	[24]
$e^- + O_2^+ \rightarrow e^- + O^+ + O$	Dissociation ion	[30]
$e^- + O_2^+ \rightarrow 2O$	Dissociative ion attachment	[31]
$e^- + O_2 \rightarrow O + O^-$	Dissociative attachment 1 O_2	[32]
$e^- + O_2 \rightarrow e^- + O^+ + O^-$	Dissociative attachment 2 O_2	[33]
$O^- + O \rightarrow e^- + O_2$	Detachment 1	[33]
$e^- + O^- \rightarrow 2e^- + O$	Detachment 2	[34]
$O^- + O_2^+ \rightarrow O + O_2$	Neutralization 1	[33]
$O^- + O_2^+ \rightarrow 3O$	Neutralization 2	[33]
$O^- + O^+ \rightarrow 2O$	Neutralization 3	[33]
$e^- + O_2 \rightarrow e^- + O_2(a^1\Delta_g)$	Generation singlet	[33]
$e^- + O_2(a^1\Delta_g) \rightarrow 2e^- + O_2^+$	Ionization singlet	[33]
$e^- + O_2(a^1\Delta_g) \rightarrow O^- + O$	Dissociative attachment singlet	[33]
$e^- + O_2(a^1\Delta_g) \rightarrow e^- + 2O$	Dissociation singlet	[33]
$e^- + O_2(a^1\Delta_g) \rightarrow e^- + O_2$	Collisional relaxation singlet	[33]
$O^- + O_2(a^1\Delta_g) \rightarrow O_2^- + O$	Charge exchange singlet	[33]
$O_2^- + O \rightarrow O^- + O_2$	Charge exchange O	[33]
$O_2^- + O_2(a^1\Delta_g) \rightarrow e^- + 2O_2$	Detachment singlet	[33]
$O_2^- + O_2^+ \rightarrow 2O_2$	Neutralization 4	[33]
$O_2^- + O^+ \rightarrow O_2 + O$	Neutralization 5	[33]
$O_2^+ + \text{Wall} \rightarrow O_2$	Surface recombination O_2^+	[16]
$O^+ + \text{Wall} \rightarrow O$	Surface recombination O^+	[16]
$O + \text{Wall} \rightarrow \frac{1}{2}O_2$	Surface recombination O	[16]

species inside the plasma and even more (chemical) reactions between them. A description of the corresponding plasmas is possible by global models [35, 36], but requires the theoretical and experimental provision of underlying microscopic parameters such as reaction cross sections etc.

The global model described was originally developed to simulate gridded ion thrusters. With minor adjustments, it can also be applied to describe rf-neutralizers in diffusion mode which was demonstrated in Ref. [15]. The electron current emitted from the rf-neutralizer is approximated by the collector current, which is given by

$$I_{\text{collector}} = h_L e A_{\text{collector}} \sum_i n_i u_{\text{B},i}, \tag{1}$$

where h_L is the edge-to-center plasma density ratio at the front face of the cylindrical discharge chamber, e is the elementary charge, $A_{\mathrm{collector}}$ is the surface area of the collector, n_i is the density of one of the positively charged plasma species and $u_{\mathrm{B},i}$ is the corresponding Bohm velocity. This collector current is considered to be equal to the electron current leaving the rf-neutralizer. The ion transparency of the neutralizer orifice is assumed to be zero, due to the negative bias applied to the orifice plate, which also functions as the ion collector.

Results

Thruster

Figure 5 shows the results of the plume measurement on the RIT-10 operated with nitrogen, oxygen, or various mixtures of both gases. These beam measurements are intended to illustrate the complexity of the plasmas of mixtures of both molecular gases and thus the necessary understanding of the individual processes of the individual gases. During

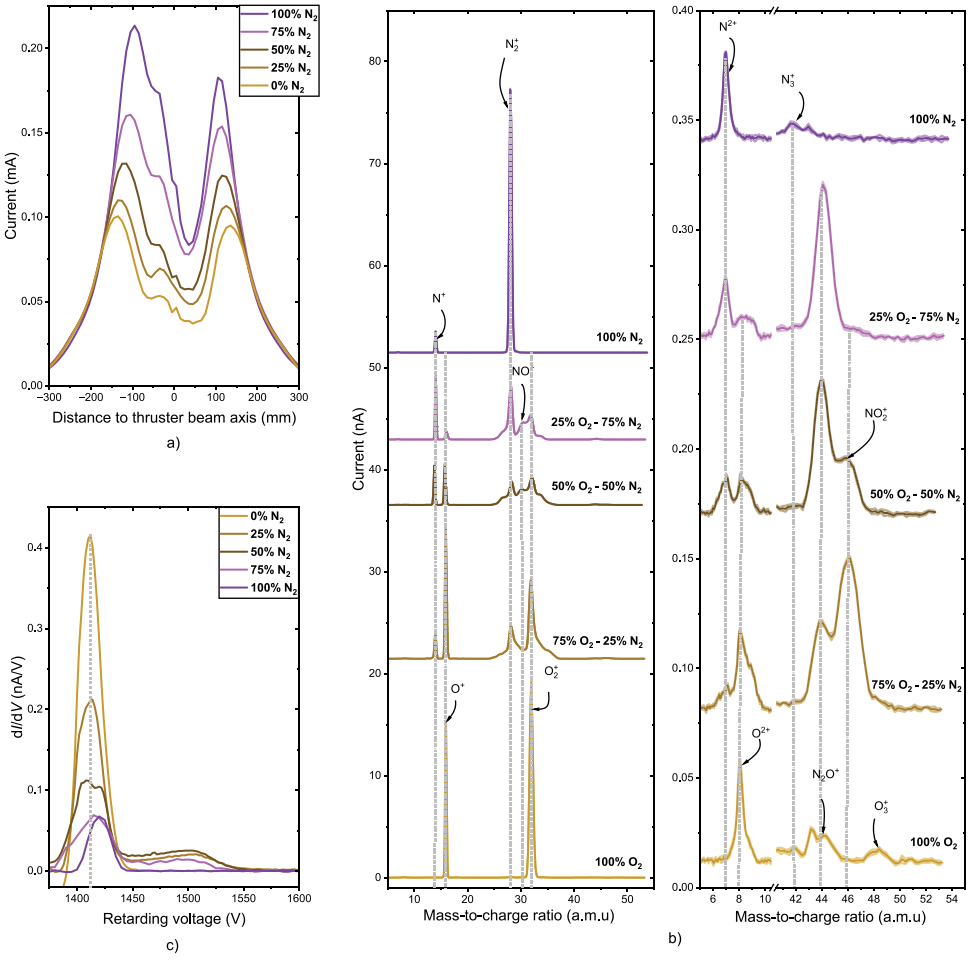

Fig. 5 Experimental results in the plume region for a beam current of 125 mA, an extraction voltage of 1400 V (first grid), and a constant mass flow rate of 7 sccm, obtained for different oxygen/nitrogen gas mixtures. (**a**) Beam profiles measured using a faraday cup reveal the effect of gas composition on spatial ion distribution. (**b**) Mass spectra obtained by magnetic sector analysis demonstrate changes in plume composition with increasing oxygen content, including distinct peaks for O^+, O_2^+, and N^+. (**c**) Ion energy distributions recorded with an rpa show the influence of molecular dissociation and charge state on peak positions

all measurements, the beam current was kept constant at 125 mA and the mass flow at 7 sccm.

The beam profiles (Fig. 5a) exhibit a double-peak structure for all gas mixtures instead of the typical Gaussian shape. The intensity maxima are located between the centerline and the beam edge, indicating a radially ring-shaped ion density distribution inside the plasma. Similar effects have previously been observed by Mühlich et al. [37] in near-field plume measurements of a RIT-10 using xenon, and in simulations of a RIT-1 thruster by Joshi and Heiliger [38]. The underlying cause is likely the low discharge pressure (≤ 0.002 mbar), which reduces the collision frequency between electrons and neutrals. This leads to increased electrical conductivity and higher electron drift velocities [39]. As a result, the skin depth decreases, which enhances induced ring currents near the chamber edge while reducing them at the center. The consequence is an "M"-shaped ion density profile along a line across the exit plane, which is also reflected in the beam shape. At higher mass flow rates, the typical Gaussian profile reappears, ruling out grid defects and supporting the explanation given above.

The beam profile has a significant impact on thrust efficiency: a more divergent ion beam, while maintaining a constant total beam current, results in reduced axial momentum transfer and thus lowers overall efficiency. Variations in the beam profile for different operating conditions further imply that single-channel diagnostic instruments (e.g., a Faraday cup) positioned at a fixed location within the plume may not provide a representative measurement of the total beam current when using this type of molecular propellant. Consequently, the mass spectrometer depicted in Fig. 2 may not sample at the plume's intensity maximum, potentially leading to a reduced signal-to-noise ratio and thus less accurate measurement results. Additionally, the composition (and ion energy) may vary between the position of maximum ion density and that at the center of the thruster. Consequently, it will be imperative to measure all plume parameters radially resolved in future studies.

From the data, the beam divergence increases from approximately 20° (nitrogen) to 28° (oxygen). This is noteworthy because the measured ion loss currents at the second grid are significantly higher for nitrogen (4–10%) compared to oxygen (2–3%). This suggests either a focusing mismatch (over-focusing for oxygen or under-focusing for nitrogen) or a higher rate of charge exchange (CEX) processes with nitrogen. Additional evidence - such as strong discoloration of the second grid on the downstream side and Faraday cup measurements perpendicular to the plume - supports the latter hypothesis.

The mass spectra (Fig. 5b) are taken along the beam axis due to constraints in the experimental setup. For noble gas propellants, typically only two ion species are observed in RIT plumes: predominantly singly charged ions and a small fraction of doubly charged ions, while the occurrence of triply charged ions is highly unlikely. In contrast, molecular propellants lead to a much greater variety of species in the plume, including singly charged atoms and molecules, doubly charged atoms (and possibly a minor fraction of doubly charged molecules), as well as some tri-atomic species. When using molecular propellant mixtures - such as oxygen-nitrogen mixtures - additional combinations of the aforementioned species originating from both propellants can be observed as well as mixed species such as NO_2^+ arising from chemical reactions inside the plasma. These circumstances further increase the spectral and compositional complexity of the plume.

The data shows, that doubly charged atoms are very unlikely (relative proportion below 1%) for all O_2/N_2 mixtures studied, including pure oxygen and pure nitrogen. For the pure gases the fraction of singly charged atoms could be determined to approximately 5% for nitrogen and 25% for oxygen at an operating point with a beam current of 125 mA and a mass flow of 7 sccm. The species fractions are determined by dividing the area of each respective peak by the total integrated signal and subsequently correcting the values for pressure-dependent charge exchange (CEX) processes and beam path scattering effects [40]. It was further assumed, that the production of doubly charged molecules is negligible.

The higher dissociation rate of oxygen compared to nitrogen measured in the experiment is consistent with their molecular bond energies: the oxygen double-bond (O = O) has a dissociation energy of 4.94 eV, whereas the nitrogen triple-bond (N≡N) requires 9.76 eV to dissociate.

When operating with mixtures of both gases at the same operating point, the molecular dissociation rate increases significantly. For example, the ATOX fraction rises from 25% to 41%, while the atomic nitrogen fraction increases from 5% to 31%. This enhanced dissociation in gas mixtures is most likely driven by Penning ionization, dissociation of tri-atomic species, or a combination of both mechanisms. Additionally, the degree of dissociation—and consequently the atomic-to-molecular ratio—increases with higher beam current, which corresponds to increased input power. The total concentration of tri-atomic species such as N_2O, NO_2, N_3 and O_3 remains consistently around 2% at this operating point, whereas the nitric oxide (NO) fraction reaches approximately 20%.

The presence of multiple ion species and concurrent physical processes highlights the increased complexity of using molecular propellants compared to noble gases, complicating performance evaluation. In particular, with regard to the generated thrust - which is directly related to the extracted ion mass via $T \propto \sqrt{m_{\mathrm{ion}}}$ - accurate characterization of the beam composition is essential across all thruster operating conditions.

Figure 5c presents the measured ion energy distributions obtained from RPA measurements. For pure nitrogen and oxygen, the ion energy distributions exhibit a single peak slightly above the screen grid potential of 1400 V, consistent with observations for noble gas propellants. In contrast, when using gas mixtures, a pronounced broadening of the energy distribution toward higher energies is observed, with ion energies exceeding the nominal acceleration potential. Specifically, energies up to 1550 eV were measured despite an applied acceleration voltage of only 1400 V, indicating the presence of additional processes within the plume. The dissociation of ions of tri-atomic molecules (N_2O, NO_2, N_3, O_3) - which were already seen in the mass spectra - shortly after extraction may lead to an energy redistribution among the dissociation products (e.g. $N_2O^+ \rightarrow N_2 + O^+$ or $N_2^+ + O$), possibly giving the ionic dissociation product a kinetic energy corresponding to distinctly higher or lower energy values than that of the educt ion.

A separate measurement conducted closer to the thruster (0.9 m instead of 3 m) confirmed this behavior. It revealed two distinct peaks: one at lower energy (1340 eV) and one at higher energy (1512 eV), symmetrically spaced around a mean of 1428 eV. This observation somewhat supports the dissociation hypothesis. However, it remains unclear at present whether the dissociation occurs inside the thruster or immediately

downstream. Consequently, the extent to which this process influences the effective thrust remains still uncertain.

It should be noted, that RPA data can be affected by internal focusing effects caused by electrostatic lensing within the grids. The impact of these effects on the measurement of energy distributions can be substantial, potentially resulting in over- or underestimation, depending on the specific design of the RPA. In the present case, no correction function was available for the RPA used, so only relative energy comparisons were made.

This broadening of the ion energy distribution affects mass spectrometry measurements, which are momentum-dependent. As a result, the molecular peaks in the measured spectra appear broadened, reflecting the underlying energy spread of the ions. As a consequence, the broadening may lead to increased uncertainties in the evaluation process, particularly in the accurate determination of species fractions and peak assignments.

These measurements show the high complexity of O_2/N_2 mixtures. To better understand these processes all following measurements where conducted using only O_2 or N_2 separately as propellant, as indicated in the roadmap in Fig. 1.

The higher dissociation rate of oxygen compared to nitrogen is evident not only in the beam mass spectra but also in the optical emission spectra inside the discharge chamber, as shown in Fig. 6. The optical emission spectrum taken of the plasma of an operating rf-neutralizer, used here as an example, closely resembles that of the plasma inside the thruster. The spectra were recorded at 1 sccm O_2 or N_2, 100 W input power, and 2 MHz excitation frequency.

In the nitrogen spectrum (Fig. 6, top), multiple molecular emission features are observed, including distinct transitions from the first and second positive systems, accompanied by several atomic lines. In contrast, the oxygen spectrum is dominated by strong atomic emission lines, with only minor contributions from molecular transitions. Notably, the overall spectral intensity is comparable in both cases. Assuming, with due caution, that the relevant transition matrix elements of molecular oxygen and nitrogen are similar, this finding suggests that the weaker molecular emission from the oxygen plasma correlates with a higher degree of dissociation of oxygen molecules inside the plasma. This correlates well with the findings from the mass spectrometry of the plume.

In order to better understand the phenomena within the plume and to improve the performance assessment of the thruster, it is essential to employ plasma diagnostics, with particular focus on Langmuir probe measurements. The evaluation of the measured data follows the approach of Nauschuett et al. [41]. However, when dealing with molecular propellants, it is imperative to consider the dissociation of the molecules in order to accurately evaluate the ion density. For evaluating the measured data, the following equations were utilized:

$$T_\mathrm{e} = \frac{2}{2k_\mathrm{B} \cdot s_\mathrm{max}}, \tag{2}$$

$$n_+ = -\frac{I_{+,\mathrm{sat}}}{0.61 A_\mathrm{p} e \sqrt{k_\mathrm{B} T_\mathrm{e}}} \frac{\sqrt{2 m_\mathrm{atomic}}}{\sqrt{2} f_\mathrm{atomic} + f_\mathrm{molecular}}, \tag{3}$$

where f_atomic and $f_\mathrm{molecular}$ represent the fraction of atomic and molecular species, respectively. These fractions can be measured at each operating point using the

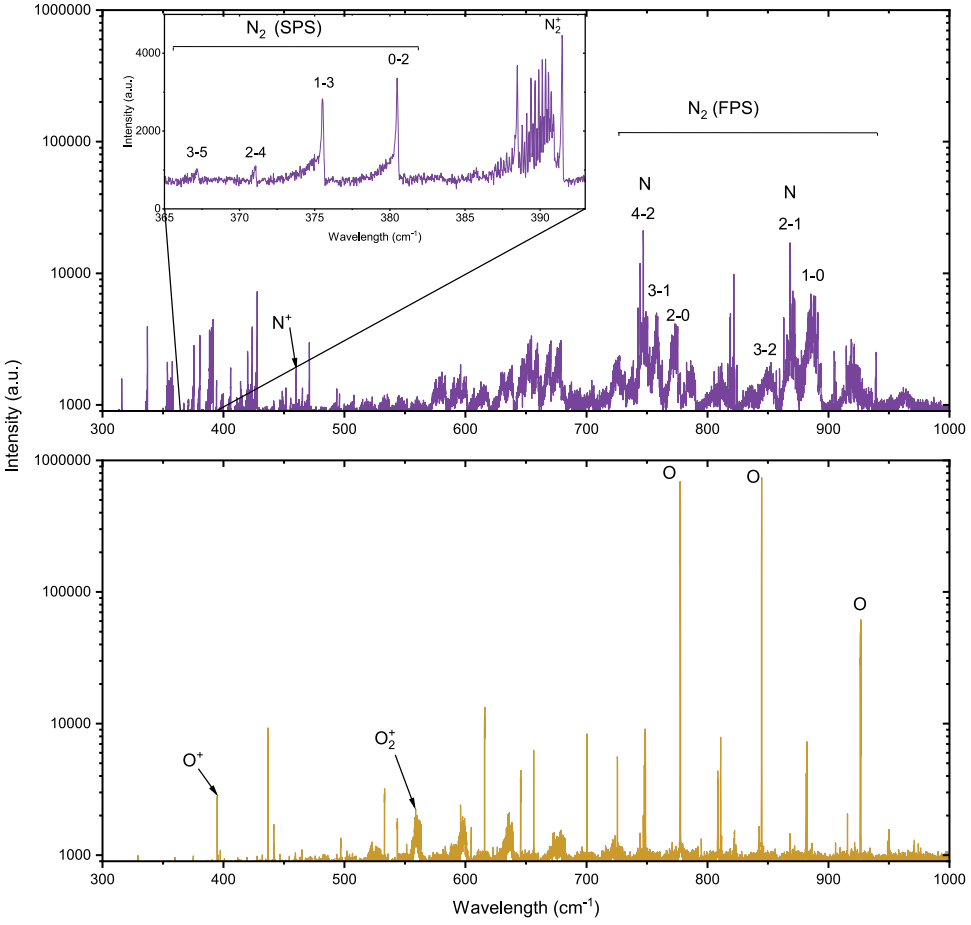

Fig. 6 Optical emission spectra of the rf-neutralizer operated at 1 sccm mass flow, 100 W input power, and 2 MHz excitation frequency. Top: spectrum recorded with pure nitrogen as operating gas. Bottom: spectrum recorded with pure oxygen as operating gas. The spectra show emission lines corresponding to neutral and ionized species, including N, N^+, N_2, O, O^+, and O_2^+, reflecting differences in dissociation and ionization behavior between the two gases

magnetic sector analyzer. It is important to note that the composition measurements are performed with ion extraction, whereas the Langmuir probe measurements can only be conducted without ion extraction. We assume, that the fractions are not significantly affected by the extraction process. $s_{\max}$ denotes the maximum slope of the fitted third-order polynomial function [41].

In the interest of simplicity, the measurements were conducted exclusively for pure nitrogen and pure oxygen. This approach was adopted due to the fact that the number of species increases considerably when oxygen-nitrogen mixtures are considered and as a consequence the evaluation of Langmuir probe measurements becomes significantly more complex.

As illustrated in Fig. 7, the input power for the thruster is maintained at constant levels either of 100 or 120 W, while the mass flow rate of pure oxygen and pure nitrogen is varied from 6 to 20 sccm. At each operating point, four Langmuir probe measurements are conducted. The densities and electron temperatures presented are the mean values extracted from these four measurements, with the highlighted area denoting the statistical deviation. The deviation for oxygen is minimal, indicating highly stable operation,

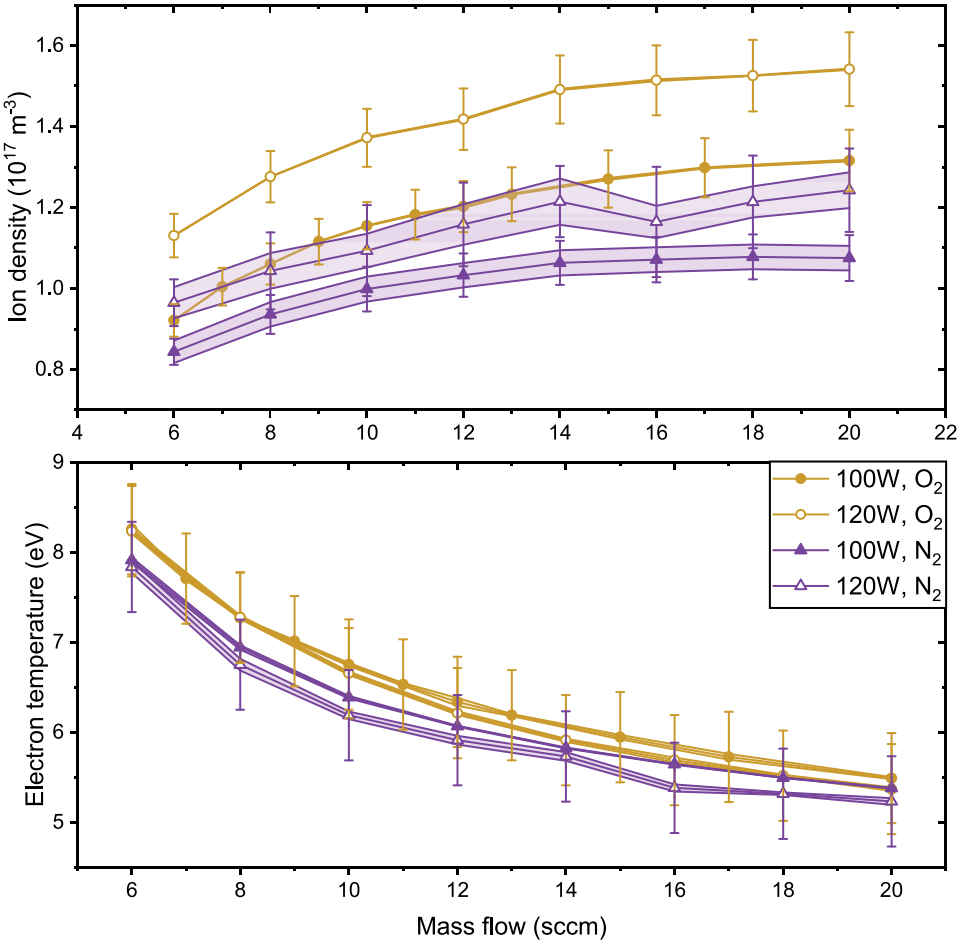

Fig. 7 Measured plasma parameters inside the RIT-10 in standby mode at 2 MHz, using pure oxygen and pure nitrogen as propellants. Top: ion density as a function of input power (100 W and 120 W) and propellant type. Bottom: corresponding electron temperature under the same conditions. The colored band defines the statistical error in multiple measurements, the error bars indicate the systematic error

whereas the deviation for nitrogen is somewhat larger, potentially attributable to instabilities or other as yet unidentified phenomena.

The conditions in the nitrogen plasma are different as is evident in the Langmuir probe current-voltage characteristic. In general, the V-I curve of a double probe characteristically exhibits a highly symmetrical shape, a property that is exemplified by the probe utilized in this study when measuring oxygen and oxygen-nitrogen mixtures. In these cases, only a minor asymmetry is observed, attributable to slight variations in the dimensions of the two pins. However, when probing a nitrogen plasma, a pronounced asymmetry becomes evident in the V-I curve. This phenomenon is attributed to alterations in the sheath layer. If the reason for this change in sheath is a non-Maxwellian electron-energy-distribution function (EEDF), the results from the nitrogen measurements need to be taken with caution, given that the Maxwellian distribution is the underlying assumption of the analysis.

Despite the error bars for nitrogen being more substantial, it is evident that the ion density for oxygen exceeds that of nitrogen at the same operating point of the thruster. This is attributable to the larger cross section for ionization for oxygen. All ion densities are found to be within the upper $10^{16}\,\mathrm{m}^{-3}$ to lower $10^{17}\,\mathrm{m}^{-3}$ range. Moreover, an

increase in input power results in a sub-linear rise in density only, a phenomenon that is also observed in case of increasing mass flow rate.

The data suggests, that the electron temperature (T_e) - which is measured to be between 5 to 8 eV - is virtually independent of both the input power and the type of propellant in the parameter range studied. Based on electron temperature T_e, the degradation of different materials that are in direct contact with the plasma can be estimated. The potential drop from the bulk plasma to the walls (in this case, the screen grid) can be derived using the following formula:

$$\phi = \frac{T_\mathrm{e}}{2} + T_\mathrm{e} \ln\left(\sqrt{\frac{M}{2\pi m_\mathrm{e}}}\right). \tag{4}$$

The potential drop, in a first approximation, is proportional to the energy of the ions impacting the screen grid. For the operating points presented in this work, this ion energy should be between 25 eV and 40 eV for both propellants and all input powers studied. The grid system of the thruster in use is made of titanium. In consideration of the sputter threshold of titanium, which is approximately 18 eV for both gases, it can be readily concluded that the grid will likely be eroded during operation of the thruster. However, using carbon or tungsten grids would be considered safe in terms of physical sputtering due to their higher sputter threshold, whereas molybdenum grids could only be employed safely in the high mass flow, low electron temperature operating points. In this consideration, we have not accounted for the chemical reactivity of the species inside the plasma. Resulting chemical assistance in the sputtering process may cause significant erosion despite ion energies being lower than the physical sputter threshold. Especially the high chemical reactivity between carbon and oxygen results in a high material degradation despite ion energies below the sputter threshold.

Neutralizer

The neutralizer was investigated by measuring the extracted electron (and negative ion) current for different mass flow rates and excitation frequencies at a constant input power of 100 W. The plasma parameters inside the discharge chamber were measured at the same time. Given that the applied voltage on the catcher was 0 V, it was possible to conduct performance measurements and Langmuir measurements simultaneously, other than for the thruster.

Since no mass spectrometry measurement in the setup used is possible for the neutralizer and thus no dissociation rate can be determined, it was assumed that in a first approximation we have the same dissociation rate inside the neutralizer as inside the thruster. In order to further enhance the simplicity of the evaluation, the mean dissociation rate from the thruster measurements is utilized for each propellant. This is an assumption as a different discharge pressure regime is present for the neutralizer compared to the thruster. However, it seems justified as the overall change in dissociation rate in case of the thruster's plasma was not significant for a varying mass flow rate at a constant power level. The mean value for the fraction of ATOX is $f_\mathrm{O} = 0.25$, while the fraction of atomic nitrogen is $f_\mathrm{N} = 0.09$. Thus, Eq. 3 can be used to estimate the ion density, provided that the dissociation rate does not change significantly when changing the frequency.

The impact of the applied excitation frequency on the ion density can be seen in the top graph of Fig. 8. It has been demonstrated that there is a strong correlation between the increase in frequency from 1.3 to 2 MHz and the increase in ion density for both gases. This increase is particularly evident in the case of nitrogen, where the rise in ion density is equivalent to the increase in frequency. Additionally, a wider mass flow range can be used due to a more efficient ionization and less excitation losses inside the plasma. For the same frequency oxygen has a higher ion density than nitrogen - a value of $7 \times 10^{17}\,\mathrm{m}^{-3}$ compared to $4 \times 10^{17}\,\mathrm{m}^{-3}$ - due to the slightly higher ionization cross section, as was already discussed for the thruster. As a rule of thumb, in order to achieve the most efficient operation, the excitation frequency f_{RFG} should be equivalent to half of the electron-neutral collision frequency $\nu_{\mathbf{e}}$:

$$f_{\mathrm{RFG}} = 0.5 \cdot \nu_{\mathbf{e}} = \frac{\overline{v}_{\mathrm{e}}}{2 \cdot \lambda_{\mathrm{e}}}. \tag{5}$$

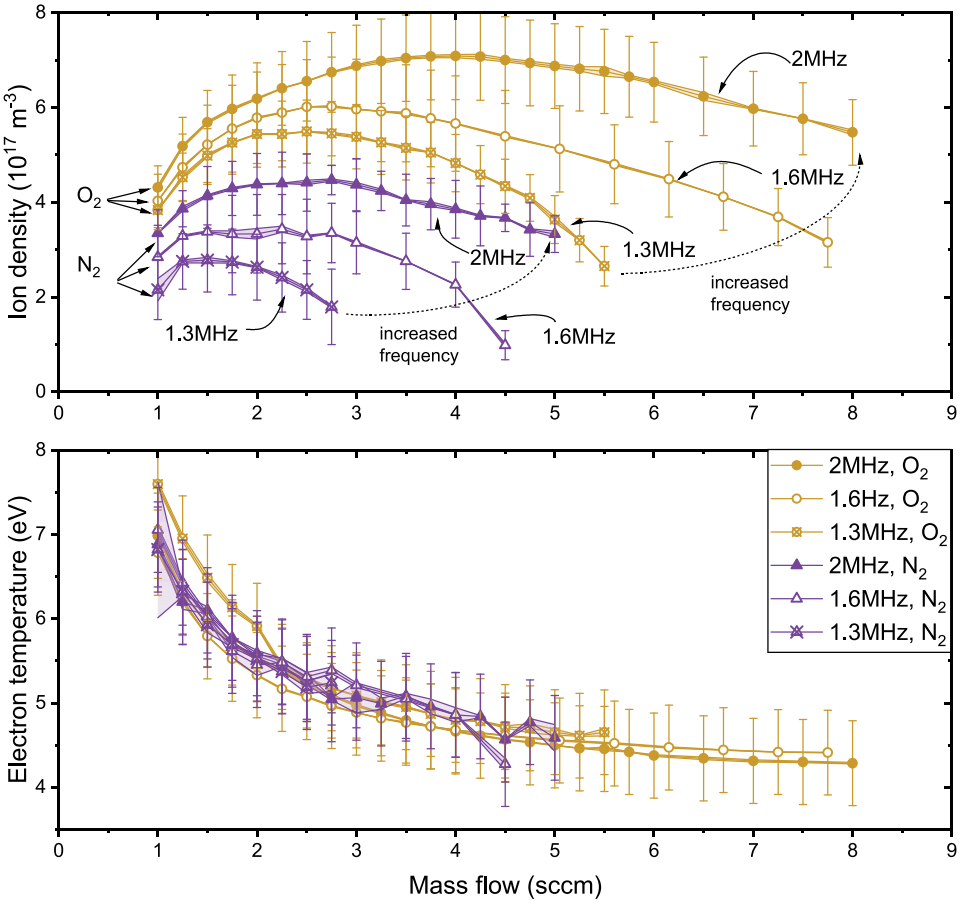

Fig. 8 Plasma parameters measured inside the rf-neutralizer at constant input power (100W), anode voltage (+35V), and ground potential at the ion catcher. Top: ion density of nitrogen and oxygen at three excitation frequencies, showing a strong dependence on frequency and mass flow. Bottom: electron temperature as a function of frequency and mass flow rate. The colored band defines the statistical error in multiple measurements, the error bars indicate the systematic error. At lower mass flows, a slight increase in T_{e} is observed for both gases, suggesting reduced collisional energy losses. Additionally, operation at lower frequencies appears to require slightly higher power absorption, possibly due to reduced coupling efficiency. These trends highlight the combined influence of excitation frequency and neutral density on plasma behavior

f_{RFG} is the excitation frequency applied, $\overline{v}_{\mathrm{e}}$ the mean electron velocity and λ_{e} the mean free path of the electrons. If the condition given by Eq. 5 is fulfilled, the majority of the electrons will have collided with a neutral particle by the end of half an rf-period, after gaining enough energy for ionization.

It follows, that in order to optimize the overall efficiency and performance of the rf-neutralizer by fulfilling Eq. 5, excitation frequencies within the range of 26 MHz to 93 MHz would be required, given the specified neutral densities inside the neutralizer. Due to a higher free mean path inside the thruster, the required frequency for optimizing the thruster performance is around 13.56 MHz. The current limitation for the radio-frequency generator used is 2 MHz. Consequently, the testing of higher frequencies was not possible. Nevertheless, this provides an opportunity for the enhancement of performance in the future.

As shown in the bottom graph of Fig. 8, the electron temperature remains unresponsive to the applied excitation frequency. A more significant influence has the pressure inside the discharge chamber, which is mainly dependent on the mass flow rate. Thus, when increasing the excitation frequency to increase the ionization, the electron temperature, and thus sputter processes at the catcher materials, remain unaffected.

The same conclusion can be drawn for the catcher materials as for the grid material. Provided that no negative voltage is applied to the catcher, it is reasonable to conclude that both tungsten and graphite would be suitable materials to use as catcher materials in terms of physical sputter erosion. However, due to increased chemical reactions between oxygen and graphite, the latter should be avoided as grid or catcher material.

The impact of the applied frequency is also evident in the current extracted from the neutralizer (Fig. 9). A higher frequency leads to a larger extracted current for the same input power, due to less excitation losses. This was already observed for a RIT-10 using iodine as propellant, while the impact of the applied frequency for xenon as propellant was very small [42].

Contrary to the observations reported by He et al. [43], no abrupt increase in extracted current was detected during variations in mass flow for a constant input power. This finding suggests that no extraction mode transition occurred within the operational

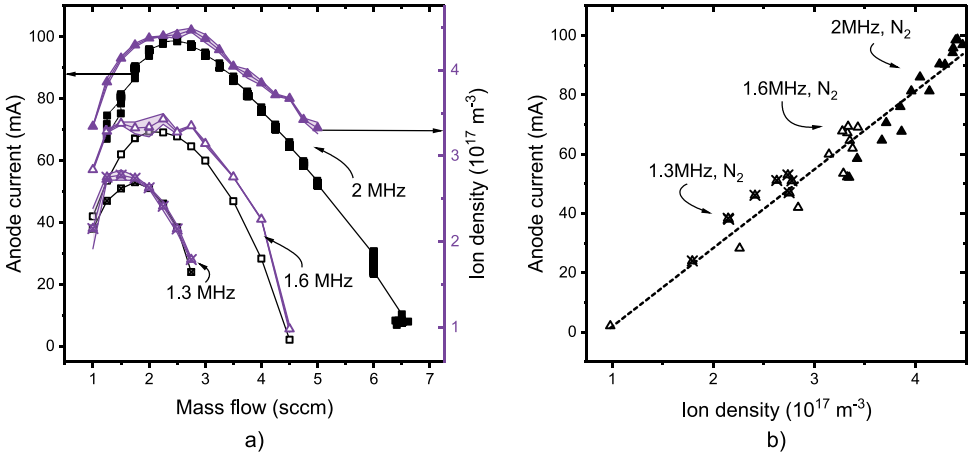

Fig. 9 Comparison of the measured ion density and the collected ion current at the anode for nitrogen. (**a**) Anode current and ion density for different mass flow rates and different frequencies. For better clarity only the statistical error of the Langmuir measurement is shown (colored band). (**b**) Correlation between anode current and ion density for all frequencies

range studied, indicating that the observed behavior is solely attributable to the applied frequency.

Furthermore, with the currently chosen neutralizer configuration with seven extraction holes, each with a diameter of 3.5 mm, a double layer sheath should form near the anode, resulting in a cylindrical rod shaped anode spot inside the discharge chamber with a theoretical amplification of the extraction current by a factor of 3–5 [43]. It has been demonstrated that a reduction in the number of holes or the orifice diameter will result in a transformation of the double layer sheath into an electron sheath. This, in turn, will lead to the formation of a spherical anode spot, which has the potential to increase the current by a factor of 10 compared to its original value. However, this hypothesis could not be substantiated in the present series of experiments. Even by increasing the anode voltage, where theoretically a sudden increase in current should be observable at a certain voltage, the current increased almost linearly until it reached a saturation point.

Given that the anode is positioned at a distance of 11 cm from the neutralizer exit, the existence of an anode spot is questionable. Also, the use of a conductive orifice plate instead of a ceramic plate may influence the creation of the anode spot mode so that the required conditions given in Ref. [43] are not fulfilled. The conditions may have to be adopted in case of a conductive orifice plate in order to achieve optimal device operation. The extraction behavior found together with a strong discoloration of the anode and the orifice plate, suggests the occurrence of additional ionization between the orifice plate and the anode, indicating the presence of a plasma bridge between the neutralizer and the anode.

A comparison of the extracted current with the measured ion density in the discharge chamber reveals that both exhibit very similar trends as a function of excitation frequency and mass flow. A linear correlation between density and extracted current is observed. Furthermore, an increase in mass flow rate results in an initial rise in current, which subsequently declines due to substantial excitation losses. This behavior was already observed by Dietz et al. [15] using the molecular propellant iodine in an rf-neutralizer, but with a constant extraction current instead of a constant input power.

With an anode voltage of 35 V in a distance of 11 cm and a catcher voltage of 0 V an maximum current of 100 mA can be extracted at 2 MHz and 100 W. By applying an additional negative catcher voltage the extracted current can be further increased. However, this operational mode can cause increased sputtering of the catcher materials.

The performance curve for the different frequencies was only studied in detail for nitrogen. The reason is that no steady state could be reached when operating the rf-neutralizer with oxygen. Utilizing oxygen results in a nearly linear decrease in the extracted current over time for a constant power input and mass flow rate. After four hours of operation at a constant operating point, the extracted current decreased from approximately 170 mA on both the catcher and anode to 140 mA on the catcher and 130 mA on the anode. For nitrogen as propellant, stable operation with a constant extraction current was possible for several hours. Hence, the most plausible explanation for this phenomenon is an oxidation of catcher and anode materials in case of oxygen as propellant. By forming non-conductive oxide layers on the surface of the orifice plate, which serves as ion catcher in this setup, the collector (and anode) area decreases and thus, according to Eq. 1, the extraction current decreases.

To investigate the severity of the oxidation process depending on the material, two different orifice plates, one made of titanium and one made of molybdenum, were used and operated with oxygen as propellant for four hours each. Before and after operation, the plates were investigated by Raman spectroscopy.

The results are shown in Fig. 10. For the titanium plate a strong oxidation is visible, especially in the center of the plate. The Raman spectra reveal, that rutile TiO_2 has formed. The one-phonon signals near 442, 612 and $826\,\mathrm{cm}^{-1}$ (with additional Raman bands near $257\,\mathrm{cm}^{-1}$ and $320\,\mathrm{cm}^{-1}$) can be assigned to E_g, A_{1g} and B_{2g} modes [44]. Typically, the formation of rutile TiO_2 would indicate temperatures above 500°C [45], but the reactive plasma conditions may lead to a formation of rutile TiO_2 at slightly lower temperatures. The predominant presence of rutile TiO_2 in the central regions supports this theory, as this area exhibits the highest ion density, thereby promoting enhanced reaction rates. The Raman signals of rutile TiO_2 decrease towards the edge, following the spherical ion density distribution inside the discharge vessel.

In contrast to the titanium plate, molybdenum oxide was detected exclusively at the edge of the corresponding orifice plate. The Raman spectra indicate that the central region remains unaffected by oxygen, while signals originating from MoO_3 and MoO_2 were observed at the edges. Due to the presence of MoO_3 with many visible modes between 200 and $400\,\mathrm{cm}^{-1}$ and the three distinct one-phonon modes at 666, 818 and $994\,\mathrm{cm}^{-1}$ (B_{2g}-, A_g- and A_g-mode) it can be assumed, that the thermodynamically stable orthorhombic $\alpha - MoO_3$-phase has formed. That indicates temperatures greater than $250\,^{\circ}\mathrm{C}$ at the edge of the plate [46]. The effect is likely more pronounced at the edge, where both inductive heating and electron temperature are significantly higher. This also shows, that Mo is stable under the plasma conditions present at the center of the orifice plate in contrast to Ti.

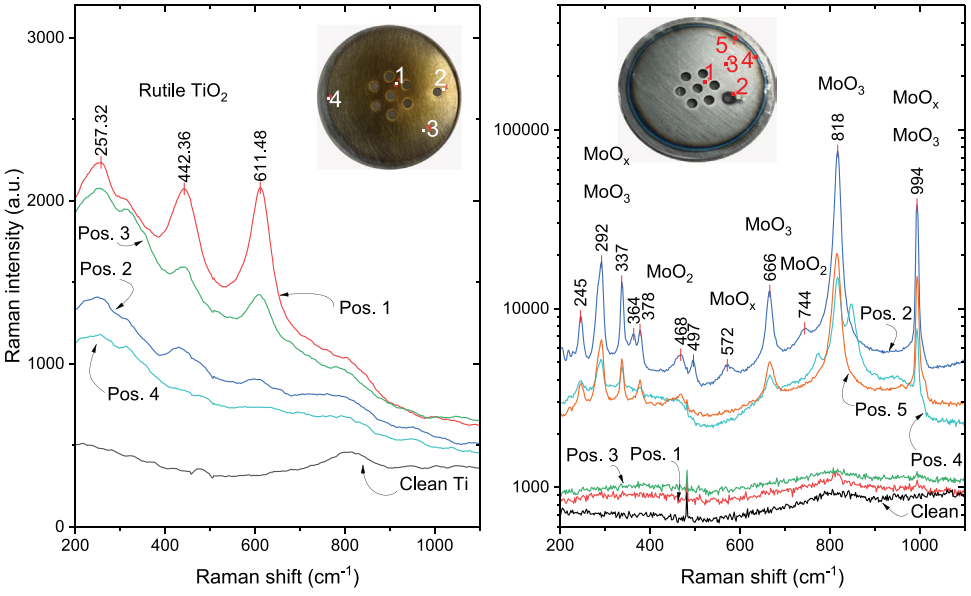

Fig. 10 Raman spectra of the two orifice plates of the neutralizer used after 4 h exposure time to an oxygen plasma. Left: titanium plate. A strong oxidation was identified across the entire surface, with the presence of rutile TiO_2 suggesting elevated neutral gas temperatures. Right: molybdenum plate. Oxidation was observed to occur only at the very edge of the plate

Furthermore. an additional oxide layer was observed on the downstream side of both orifice plates. This oxide layer covers the entire outer surface. This supports the hypothesis that the neutralizer was operating in bridge mode. In this configuration, extracted and accelerated electrons can further ionize the neutral gas between the neutralizer and the anode. As a result, positively charged oxygen ions are accelerated back towards the plate, leading to oxide layer formation and sputtering of the downstream surface due to an increased impact energy.

The thruster's grid system is also composed of titanium; however, it did not experience the same extent of oxidation as the neutralizers titanium orifice. As will be discussed in detail later, this difference is attributed to the lower pressure within the discharge chamber of the thruster.

Comparison of thruster and neutralizer

Figure 11 presents a comparison of the measured plasma parameters for the neutralizer and the thruster for both propellants, oxygen and nitrogen. To facilitate comparison, the mass flow was converted into an equivalent pressure within the discharge chamber. The conversion was conducted with the assistance of global models, where the flow regime

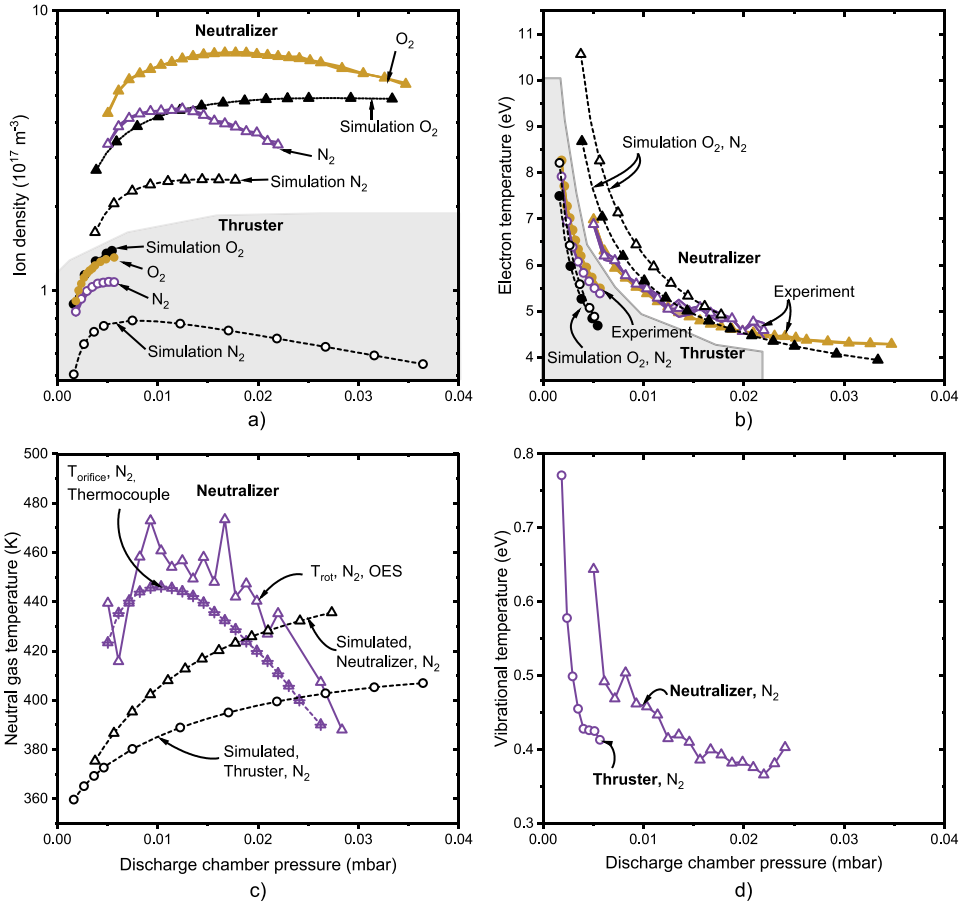

Fig. 11 Comparison of the measured and simulated plasma parameters in the thruster and neutralizer for 100 W constant input power and 2 MHz with regard to the pressure inside the discharge chamber. The grey part denotes the thruster's values. For better visibility, only the very small statistical errors are shown in all measurements. (**a**) Measured and simulated ion density. (**b**) Measured and simulated electron temperature. (**c**) Comparison of the simulated and measured neutral gas temperature inside the neutralizer and the thruster using nitrogen as operating gas. (**d**) Measured vibrational temperature of the nitrogen molecules

for both devices was assumed to be a molecular flow. This assumption is used in many global models [14, 15]. However, it should be noted, that the flow regime, especially in the case of the neutralizer, may vary from the molecular flow for certain operating points. This needs to be investigated further in future studies. However, a linear relationship was identified between the mass flow rate and the resulting discharge pressure for both systems and both gases. Linear conversion from the simulation was employed to calculate the pressure in the discharge chamber for the experiments. Thus, a comparison between the models and both devices was possible. A thorough analytical estimation was conducted using the mean thermal velocity and the neutral gas transparency of the grids. This analysis yielded equivalent values, with a maximum deviation of 13% from the calculated results derived from the simulations. Therefore, the maximum allowable error was determined to be 20% for all calculated discharge pressures. The resulting discharge pressure range for both systems is currently mainly limited by the used radio-frequency generator and the thermal design of the current laboratory prototypes. Theoretically, lower pressures are still possible with a gridded ion thruster.

The experimental data are further compared with the simulations, based on the global models for oxygen and nitrogen described in Sect. 3, in terms of dissociation rate for both gases, total ion density, electron and neutral temperature for both investigated systems.

As shown in Fig. 11a, both, the Langmuir probe measurements and the simulations indicate that the ion density in the neutralizer is approximately five times higher than in the thruster. The comparison between simulation and experimental data for the thruster operating with oxygen shows very good agreement. In contrast, the simulation for nitrogen as propellant exhibits a significant deviation in absolute values, although the overall trend is reproduced correctly. This discrepancy arises from an overestimation of the molecular dissociation in the nitrogen model. While the experimental data indicate a nearly constant fraction of atomic nitrogen ions of approximately 10% across all operating points, the simulation predicts an initial fraction of 60%, which decreases to 30% with increasing mass flow rate. A higher atomic nitrogen fraction implies a reduced overall ionization degree at constant power input, due to the higher ionization energy required for atomic species compared to molecular nitrogen. These deviations clearly show that some important physical (and chemical) processes are not included in our global models yet or some of the assumed microscopic parameters are not correct. Especially the higher dissociation rate of nitrogen needs to be investigated further to have a more accurate model. A characterization of both devices for the more complex mixture of oxygen and nitrogen can be performed and compared with a global model, like in Refs. [35] and [36], only after the models for both elemental binary gases have been adjusted and improved.

Comparing the thruster and neutralizer by calculating the number of ions by multiplying the measured ion density with the volume of the discharge vessel ($3.25 \cdot 10^{-4}\,\mathrm{m}^3$ for the thruster and $7 \cdot 10^{-5}\,\mathrm{m}^3$ for the neutralizer) results in a slightly smaller number of ions for oxygen inside the thruster than in the neutralizer, but an almost equal number of ions for nitrogen for both devices.

This finding suggests that plasma generation within the neutralizer is sufficient to support a current output comparable to that of the thruster, in the range of 150–200 mA. Therefore, the current limitation of the neutralizer is attributed to the extraction process.

Further supporting the conclusion of comparable discharge chamber conditions - and thus potentially similar performance in terms of extractable maximum currents - is the observation that electron temperatures are in a similar range in both devices (Fig. 11b), although equal values occur at slightly different pressure ranges. However, the simulations reveal that the neutral gas temperature is significantly higher in the neutralizer, reaching up to $200\,^{\circ}\mathrm{C}$, whereas it remains below $130\,^{\circ}\mathrm{C}$ in the thruster.

The neutral gas temperature can be assumed to be equivalent to the rotational temperature of the molecules [47]. Given the strength of molecular band transitions in nitrogen, the rotational temperature of nitrogen molecules can be calculated from the measured optical emission spectra. With Eq. 6, taken from Britun et al. [47], where I_1 is the intensity at 775.2 nm and I_2 the intensity at 774 nm, the rotational temperature can be estimated very easily by:

$$T_{\mathrm{rot}}[\mathrm{K}] = \frac{195}{\left(\frac{I_1}{I_2} - 0.52\right)}. \tag{6}$$

The two chosen wavelengths correspond to different rotational transitions in the (2–0) oscillation band of the first positive system for nitrogen. Calculating the rotational temperature T_{r} for nitrogen inside the neutralizer yields a similar behavior as that of the measured ion density. The rotational temperature increases for increasing mass flow up to a certain point. For mass flows above this point, T_{r} decreases again (see Fig. 11c). Although not shown here, it was also observed that the rotational temperature increases slightly with increasing frequency.

T_{r} is in the range of 390 K to 480 K for an excitation frequency of 2 MHz. These measurements correlate well with temperature measurements conducted at the orifice plate using a type K thermocouple and also with the overall temperature range predicted in the simulations. Despite the matching range, the overall trend of the neutral gas temperature in dependence on the discharge chamber pressure shows strong deviations between simulated values and measured ones. This suggests that certain phenomena are not yet captured by the simulation, limiting its ability to fully describe the behavior and performance of the neutralizer.

Nevertheless, it provides a sufficiently accurate basis for an initial approximation. For oxygen, the neutral gas temperature in the simulation exhibits the same trend as observed for nitrogen and lies within a comparable temperature range. This indicates, that the neutral gas temperature is below the theoretical temperature needed to start the oxidation processes at the orifice plate. However, due to the acceleration of ions toward the wall, their impact energy is likely sufficient to induce oxidation of the material.

Additionally, it has been demonstrated that the vibrations of the diatomic molecules described by the vibrational temperature T_{v} functions as an energy reservoir, which is important for chemical reactions [48]. Pursuant to the formula for the intensity of transitions that assumes a Boltzmann distribution [49],

$$I_{\nu'\nu''} = C(\lambda) A_{\nu'\nu''} \frac{2\pi c}{\lambda} e^{-\frac{E_{\nu'}}{k_{\mathrm{B}} T_{\mathrm{v}}}}, \tag{7}$$

it can be deduced that

Table 4 Spectroscopic constants used to calculate the vibrational temperature (T_v), based on selected emission transitions [47, 50–52]

λ (nm)	$A_{\nu'\nu''}(\mathrm{Sec}^{-1})$	ν'	ν''	$G(\nu')(\mathrm{cm}^{-1})$
380.49	0.134	0	2	1016
375.54	0.185	1	3	2987
371.05	0.151	2	4	4764
367.19	0.0868	3	5	6103

$$\ln\left(\frac{I\cdot\lambda}{A_{\nu'\nu''}\cdot 2\pi c}\right) = -\frac{1}{T_\mathrm{v}}\frac{E_{\nu'}}{k_\mathrm{B}} = -\frac{1}{T_\mathrm{v}}\frac{G(\nu)\cdot h\cdot c}{k_\mathrm{B}}. \tag{8}$$

Thus, using the spectroscopic values from the four transitions of the second positive system of nitrogen listed in Table 4, where $\Delta\nu = 2$, the negative inverse of the slope of the corresponding Boltzmann plot yields T_v. The measured vibrational temperatures shown in Fig. 11d range from 0.4 eV to almost 0.8 eV and correspond to 4600 K to 9000 K. This holds for the plasma in both thruster and neutralizer. Especially in the low pressure region, the high T_v indicates a large amount of energy stored in vibrations, which decreases towards higher pressures.

This phenomenon is considerably more significant in the case of the neutralizer, given that it operates under substantially higher pressures. For low to medium pressure regions, the stored energy, thus T_v, decreases due to the increasing ionization rate. After the ionization reaches its maxima, the ion density n_i decreases again (Fig. 11a) as well as T_v (Fig. 11d), T_r (Fig. 11c) and T_e (Fig. 11b). The simulations further yield that also the dissociation of the molecules decreases with increasing mass flow rate. Since the neutralizer was operated with a constant power input the following conclusion can be drawn: More energy is used for chemical reactions and excitation of the molecules and atoms when going to higher pressures inside the discharge vessel.

This is consistent with the observation that the extracted current from the neutralizer is more stable in the low mass flow range, while at pressures higher than $0.01 - 0.015$ mbar the current starts to decrease linearly in the case of oxygen due to the increased chemical reaction rate. The decrease of T_v with higher mass flow rate is based on collision-induced relaxation due to higher pressure and faster quenching. In this process, excited molecules release their energy through collisions instead of photon emission. This released energy is then used for chemical processes and is high enough to even form rutile titania, as seen in the Raman spectra. For the thruster this is not an issue, since it is mostly operated in the very low pressure region of $0.0025 - 0.005$ mbar, where the energy storage is rather high and chemical reactions are less prevalent.

Conclusion

In this study, a RIT-10 ion thruster and an rf-neutralizer were investigated using molecular propellants - oxygen, nitrogen, and their mixtures in order to assess their suitability and potential for use in an ABEP system. Due to the complex physical and chemical behavior of reactive molecular gases compared to noble gases, it is of paramount importance to employ a wide range of diagnostics separately to fully characterize the system performance and limitations.

The results from the investigation of the single gases (O_2 and N_2 separately) demonstrate that high excitation frequencies and low mass flow rates allow for stable and efficient operation of both subsystems. Moreover, the use of robust materials such as

tungsten and molybdenum was identified as essential for extended operation with oxygen and nitrogen, based on preliminary material compatibility assessments.

It was further shown, that the RIT-10 thruster and the used rf-neutralizer both function well, even with the chemically challenging molecular propellant oxygen. Since the thruster was already tested with mixtures, it can be assumed with high likelihood, that the neutralizer will perform equally well with oxygen-nitrogen mixtures.

The milestone of our ABEP roadmap highlighted in red in Fig. 1 was achieved. The experimental characterization of both neutralizer and thruster operating with either O_2 or N_2 was successful. However, the global model shows some significant deviations in the case of nitrogen. The model for nitrogen needs to be revised and improved before the next step in the roadmap can be taken: characterizing both devices with O_2/N_2 mixtures.

In addition, a subsequent step should involve experimental investigation of an intake system. In the case that the intake delivers the required performance (e.g. sufficient mass flow and pressure) for the thruster, the entire ABEP system, consisting of the intake, RIT, and rf-neutralizer, will be assembled and tested.

These findings contribute to the further development of air-breathing electric propulsion systems for very low Earth orbit applications, where performance optimization under reactive molecular gas conditions is essential.

Acknowledgements
J.Z. is grateful for the provision of a PhD scholarship grant by the University of Giessen. P.J.K is grateful for funding in the frame of "React-EU" by the State Hesse.

Author contributions
J.Z. wrote the manuscript, prepared the figures and was mainly responsible for the experiments. A.R.W. and K.K. provided the global model and conducted the simulations. L.C. conducted the Raman spectroscopic measurements. K.H. and P.J.K. reviewed the manuscript and provided feedback. All other authors helped with the experiments and evaluation of the data.

Funding
Open Access funding enabled and organized by Projekt DEAL.

Data availability
Data that support the findings of this study have been deposited in the JLU's internal repository, JLUpub, and are available under the following link: https://jlupub.ub.uni-giessen.de/items/b62bbc5c-ed4b-4c1c-bc8a-5fe7e56af643

Declarations

Competing interests
The authors declare no competing interests.

Received: 30 May 2025 / Accepted: 21 October 2025
Published online: 12 November 2025

References

1. Andreussi T, Ferrato E, Giannetti V (2022) A review of air-breathing electric propulsion: from mission studies to technology verification. J Educ Chang Electric Propul 1(1). https://doi.org/10.1007/s44205-022-00024-9
2. Andreussi T, Ferrato E, Paissoni CA, Kitaeva A, Giannetti V, Piragino A, Schäff S, Katsonis K, Berenguer C, Kovacova Z, Neubauer E, Tisaev M, Karadag B, Lucca Fabris A, Smirnova M, Mingo A, Le Quang D, Alsalihi Z, Bariselli F, Parodi P, Jorge P, Magin TE (2022) The aether project: development of air-breathing electric propulsion for VLEO missions. CEAS Space J 14(4):717–740. https://doi.org/10.1007/s12567-022-00442-3
3. Zheng P, Wu J, Zhang Y, Wu B (2020) A comprehensive review of atmosphere-breathing electric propulsion systems. Int J Aerosp Eng 1–21. https://doi.org/10.1155/2020/8811847
4. Adkins C, Belcher D, Akhter M, Duggleby A, Cardwell ND, Staack D (2024) Design and optimization of a high thrust density air-breathing pulsed plasma thruster array. J Educ Chang Electric Propul 3(1). https://doi.org/10.1007/s44205-024-00071-4
5. Zheng P, Wu J, Zhang Y, Che B, Zhao Y (2023) An atmosphere-breathing propulsion system using inductively coupled plasma source. Chin J Aeronaut 36(5):223–238. https://doi.org/10.1016/j.cja.2023.03.003
6. Tisaev M, Karadag B, Masillo S, Lucca Fabris A (2023) Performance and plasma diagnostics of the air-breathing microwave plasma CAThode (AMPCAT) coupled to a cylindrical Hall thruster. J Appl Phys 134(19). https://doi.org/10.1063/5.0176682

7. Herdrich G, Papavramidis K, Maier P, Skalden J, Hild F, Beyer J, Pfeiffer M, Fugmann M, Klinker S, Fasoulas S, Souhair N, Ponti F, Walther M, Wiegand A, Walpot L, Duesmann B, Borras EB, Roberts PCE, Crisp NH (2024) System design study of a VLEO satellite platform using the IRS RF helicon-based plasma thruster. Acta Astronautica 215:245–259. https://doi.org/10.1016/j.actaastro.2023.11.009
8. Shabshelowitz A, Gallimore AD, Peterson PY (2014) Performance of a Helicon Hall thruster operating with xenon, argon, and nitrogen. J Propul Power 30(3):664–671. https://doi.org/10.2514/1.b35041
9. Hu P, Shen Y, Yao Z, Mao W, Hu Y, Liu X (2021) Study of multi-cusped plasma thruster applied to air-breathing electric propulsion. Vacuum 190, 110275. (https://doi.org/10.1016/j.vacuum.2021.110275
10. Rabunal-Gayo A, Fajardo P, Inchingolo MR, Navarro-Cavallé J (2024) Status review of air breathing electric propulsion experimental research at UC3M. In International Electric Propulsion Conference, IEPC-2024-773, Toulouse, France.
11. Andreussi T, Cifali G, Giannetti V, Piragino A, Ferrato E, Rossodivita A, Andrenucci M, Longo J, Walpot L (2017) Development and experimental validation of a Hall effect thruster RAM-EP concept. International Electric Propulsion Conference, IEPC-2017-377, Atlanta, Georgia – USA.
12. Scholze F, Tartz M, Neumann H (2008) Inductive coupled radio frequency plasma bridge neutralizer. Rev Sci Instrum 79(2). https://doi.org/10.1063/1.2802587
13. Gurciullo A, Fabris AL, Knoll A (2017) Alternative neutralization technologies enabling the use of exotic propellants in electric propulsion. In International Electric Propulsion Conference, IEPC-2017-251, Atlanta, Georgia – USA.
14. Dietz P, Reeh A, Keil K, Holste K, Probst U, Klar PJ, Volkmar C (2021) Global models for radio-frequency ion thrusters. EPJ Tech Instrum 8(1). https://doi.org/10.1140/epjti/s40485-021-00068-5
15. Dietz P, Becker F, Keil K, Holste K, Klar PJ (2020) Performance of a RF neutralizer operating with noble gases and iodine. Eur Phys J D Appl Phys 91(1), 10901 https://doi.org/10.1051/epjap/2020190213
16. Grondein P, Lafleur T, Chabert P, Aanesland A (2016) Global model of an iodine gridded plasma thruster. Phys Plasmas 23(3). https://doi.org/10.1063/1.4944882
17. Chabert P, Arancibia Monreal J, Bredin J, Popelier L, Aanesland A (2012) Global model of a gridded-ion thruster powered by a radiofrequency inductive coil. Phys Plasmas 19(7). https://doi.org/10.1063/1.4737114
18. Biagi Database. Fortran program, MAGBOLTZ, S. F. Biagi, version 8.97. lxcat.net. (Last checked: 2023-05-19)
19. Wang Y, Zatsarinny O, Bartschat K (2014) B-spline R-matrix-with-pseudostates calculations for electron-impact excitation and ionization of nitrogen. Phys Rev A 89(6), 062714. https://doi.org/10.1103/physreva.89.062714
20. Itikawa Y (2005) Cross sections for electron collisions with nitrogen molecules. J Phys Chem Ref Data 35(1). https://doi.org/10.1063/1.1937426
21. Bahati EM, Jureta JJ, Belic DS, Cherkani-Hassani H, Abdellahi MO, Defrance P (2001) Electron impact dissociation and ionization of N^+_2. J Phys B: At Mol Opt Phys 34(15). https://doi.org/10.1088/0953-4075/34/15/303
22. Cosby PC (1993) Electron-impact dissociation of nitrogen. J Chem Phys 98(12). https://doi.org/10.1063/1.464385
23. Thorsteinsson EG, Gudmundsson JT (2009) A global (volume averaged) model of a nitrogen discharge: I. Steady state Plasma Sources Sci Technol 18(4). https://doi.org/10.1088/0963-0252/18/4/045001
24. Alves LL (2014) The IST-LISBON database on LXCat. J Phys Conf Ser 565(1), 012007. https://doi.org/10.1088/1742-6596/565/1/012007
25. Morgan Database. lxcat.net. (Last checked: 2023-05-19)
26. Itikawa Y (2008) Cross sections for electron collisions with oxygen molecules. J Phys Chem Ref Data 38(1). https://doi.org/10.1063/1.3025886
27. Alves LL, Coche P, Ridenti MA, Guerra V (2016) Electron scattering cross sections for the modelling of oxygen-containing plasmas. Eur Phys J D 70(6). https://doi.org/10.1140/epjd/e2016-70102-1
28. Stepanek J (2003) Electron and positron atomic elastic scattering cross sections. Radiat Phys Chem 66(2). https://doi.org/10.1016/s0969-806x(02)00386-9
29. Laher RR, Gilmore FR (1990) Updated excitation and Ionization cross sections for electron impact on atomic oxygen. J Phys Chem Ref Data 19(1). https://doi.org/10.1063/1.555872
30. Cherkani-Hassani H, Belic DS, Jureta JJ, Defrance P (2006) Absolute cross sections for electron impact ionization and dissociation of O^+_2. J Phys B: At Mol Opt Phys 39(24). https://doi.org/10.1088/0953-4075/39/24/008
31. Lieberman MA (2005) Principles of plasma discharges and materials processing. Wiley-Interscience, Hoboken (New Jersey)
32. Gudmundsson JT, Lieberman MA (1998) Model and measurements for a planar inductive oxygen discharge. Plasma Sources Sci Technol 7(1). https://doi.org/10.1088/0963-0252/7/1/002
33. Kim S, Lieberman MA, Lichtenberg AJ, Gudmundsson JT (2006) Improved volume-averaged model for steady and pulsed-power electronegative discharges. J Retailing Vac Sciamp; Technol A: Vac, Surfaces, and Films 24(6). https://doi.org/10.1116/1.2345645
34. Corr CS, Gomez S, Graham WG (2012) Discharge kinetics of inductively coupled oxygen plasmas: experiment and model. Plasma Sources Sci Technol 21(5). https://doi.org/10.1088/0963-0252/21/5/055024
35. Mrózek K, Dytrych T, Moliš P, Dániel V, Obrusník A (2021) Global plasma modeling of a magnetized high-frequency plasma source in low-pressure nitrogen and oxygen for air-breathing electric propulsion applications. Plasma Sources Sci Technol 30(12), 125007. https://doi.org/10.1088/1361-6595/ac36ac
36. Šťastný M, Mrózek K, Juřík K, Havlíček L, Novotný M, Obrusník A (2024) Numerical simulations of a low-pressure electrodeless ion source intended for air-breathing electric propulsion. J Phys D: Appl Phys 57(49), 495203. https://doi.org/10.1088/1361-6463/ad7471
37. Mühlich NS, Holste K, Klar PJ (2017) Near-field beam diagnostics for radio-frequency ion thrusters RIT. In IEPC-2017-476, International Electric Propulsion Conference, Atlanta, Georgia – USA
38. Joshi N, Heiliger C (2024) Particle-in-cell simulation of radio-frequency ion thruster RIT-1.0. J Educ Chang Electric Propul 3(1). https://doi.org/10.1007/s44205-024-00067-0
39. Reeh A (2021) Der Modellierungsprozess und die Auslegung eines Radiofrequenz-Ionentriebwerks: ein Simulationstool zur Untersuchung des Plasmas, der Ionenoptik, der induktiven Leistungseinkopplung und der Hochfrequenzgenerierung sowie deren verkoppelten Verhaltens. PhD thesis. https://doi.org/10.22029/JLUPUB-9844
40. Zorn J, Forchheim O, Holste K, Klar PJ (2025) Challenges using rarefied atmospheric gases as propellant for an RAM-EP system. In Proceedings of the 33rd International Symposium on Rarefied Gas Dynamics (In press)

41. Nauschütt BT, Chen L, Holste K, Klar PJ (2021) Non-invasive assessment of plasma parameters inside an ion thruster combining optical emission spectroscopy and principal component analysis. EPJ Tech Instrum 8(1). https://doi.org/10.1140/epjti/s40485-021-00070-x
42. Holste K, Gärtner W, Zschätzsch D, Scharmann S, Köhler P, Dietz P, Klar PJ (2018) Performance of an iodine-fueled radio-frequency ion-thruster. Eur Phys J D 72(1). https://doi.org/10.1140/epjd/e2017-80498-5
43. He J, Ma L, Xue S, Zhang C, Duan L, Kang Q (2018) Study of electron-extraction characteristics of an inductively coupled radio-frequency plasma neutralizer. Plasma Sci Technol 20(2), 025403. https://doi.org/10.1088/2058-6272/aa89e1
44. Kuhl F, Lu H, Becker M, Chen L, Zheng Y, Polity A, Zhang Z, He Y, Klar PJ (2024) Raman scattering of TixV1−xO2 thin films on (110) rutile TiO2 in the low and high temperature phase adjacent to the metal–insulator transition. J Raman Spectrosc 55(8):923–938. https://doi.org/10.1002/jrs.6684
45. Zhang Y, Ebbinghaus SG, Weidenkaff A, Kurz T, Nidda H-A, Klar PJ, Güngerich M, Reller A (2003) Controlled iron-doping of macrotextured nanocrystalline titania. Chem Of Mater 15(21):4028–4033. https://doi.org/10.1021/cm034246p
46. Melo O, González Y, Climent-Font A, Galán P, Ruediger A, Sánchez M, Calvo-Mola C, Santana G, Torres-Costa V (2019) Optical and electrical properties of moO_2 and moO_3 thin films prepared from the chemically driven isothermal close space vapor transport technique. J Phys Condens Matter 31(29), 295703. https://doi.org/10.1088/1361-648x/ab18e2
47. Britun N, Gaillard M, Ricard A, Kim YM, Kim KS, Han JG (2007) Determination of the vibrational, rotational and electron temperatures in N_2 and Ar–N_2 rf discharge. J Phys D: Appl Phys 40(4):1022–1029. https://doi.org/10.1088/0022-3727/40/4/016
48. Fridman A, Fridman A, Kennedy LA, Kennedy LA (2004) Plasma physics and engineering, 1st edn. CRC Press. https://doi.org/10.1201/9781482293630
49. Fatima H, Ullah MU, Ahmad S, Imran M, Sajjad S, Hussain S, Qayyum A (2021) Spectroscopic evaluation of vibrational temperature and electron density in reduced pressure radio frequency nitrogen plasma. SN Appl Sci 3(6). https://doi.org/10.1007/s42452-021-04651-z
50. Hartmann G, Johnson PC (1978) Measurements of relative transition probabilities and the variation of the electronic transition moment for $N_2C^3\Pi_u$-$B^3\Pi_g$ second positive system. J Phys B: At Mol Phys 11(9):1597–1612. https://doi.org/10.1088/0022-3700/11/9/013
51. Angus WR (1941) The identification of molecular spectra. Nature 148(3748):240–240. https://doi.org/10.1038/148240a0
52. Naveed MA, Qayyum A, Ali S, Zakaullah M (2006) Effects of helium gas mixing on the production of active species in nitrogen plasma. Phys Lett A 359(5):499–503. https://doi.org/10.1016/j.physleta.2006.07.002

Publisher's Note